Raman and Rayleigh Holographic Lidar

(as appears in Applied Optics, Vol. 41, No. 9, 1798-1804, 20 March, 2002)

Geoff Andersen, Jason K. Brasseur, R. J. Knize and Paul Haris
Laser and Optics Research Center
HQ USAFA/DFP,
Suite 2A31, 2354 Fairchild Dr.,
USAF Academy, CO 80840

Abstract

We have designed a novel rotational Raman and Rayleigh lidar system that incorporates a simple holographic optical element. The hologram simultaneously disperses and focuses the backscattered signal light so that narrow spectral features can be isolated and detected with high efficiency. By measuring relative strength of several nitrogen rotational Raman lines, an accurate temperature of the atmosphere at a given altitude can be obtained without the need for external calibration. Simultaneous photon counting of the Rayleigh backscatter signal permits temperature measurements at much higher altitudes.

OCIS Codes: 280.0280, 280.3640, 090.2890, 290.5860, 290.5870
Keywords: Remote sensing, lidar, holographic optical elements, Raman scattering, Rayleigh scattering.

1. Introduction

Lidar holds the promise of a single instrument capable of measuring precise temperature profiles of the atmosphere from ground to space. Since proposed by Cooney[1], rotational Raman lidar has been used for low-to-medium altitude thermal profilometry[2-7]. A laser pulse is directed through the atmosphere and a telescope gathers the rotational Raman scattering (RRS) spectrum backscattered by N_2 and O_2 molecules. The spectrum will have a characteristic shape dependent on the temperature of the scattering molecules. Traditionally, the shape of the spectrum is found by measuring the relative power passing through narrow-band filters centered on two discrete points of the spectrum. In order for this technique to produce reliable results, the optical characteristics must be calibrated and controlled to a high degree of precision[4]. Thermal and mechanical drifts in filter systems can cause drift in the calibration curve, and thus systematic temperature errors. In this paper we introduce the idea, based on previous work[8-10], of using a single holographic optical element (HOE) that can spatially isolate the spectral components of the nitrogen RRS spectrum such that individual lines can be extracted and detected with high efficiency with no measurable changes due to thermal drift. The absolute shape of the RRS spectrum can be determined with a single, initial calibration of the optical system prior to data collection.

Rayleigh lidar[11-14] operates by measuring the strength of the elastic backscattered component and integrating downwards through a model atmosphere using a combination of the hydrostatic and ideal gas laws. Rayleigh scattering is over 3 orders of magnitude

larger than that of the RRS, but cannot be used at low altitudes (<30km) due to signal contamination by Mie scattering from aerosols. As with any other lidar system, the maximum altitude that can be probed by this method is directly related to the number of photons that can be counted from any given layer. The HOE in our lidar system allows for the simultaneous extraction of the Rayleigh as well as the RRS signal. By combining the profiles from both the rotational Raman and Rayleigh temperature measurements, a single atmospheric profile is possible up to 60km. This is an improvement over a combined vibrational Raman/ Rayleigh lidar[15], which used conventional filtering and did not extend measurements below 8km.

A schematic diagram of the lidar system is shown in Figure 1. A pulsed laser beam is expanded and directed into the atmosphere along the axis of a telescope. The backscattered light is gathered by the telescope and focused into an optical fiber. The light exiting the transport fiber is collimated and directed onto a holographic optical element that simultaneously focuses and disperses the light into separate fibers (with only the Rayleigh and two Raman lines shown here for simplicity). The holographic optical element acts like the grating in a spectrometer, with narrow frequency selectivity. The difference, however, is that the HOE can be simply fabricated in-house and, unlike most commercially available spectrometers, can allow for simultaneous photon-counting of several spectral lines, instead of scanning each one individually over a period of time.

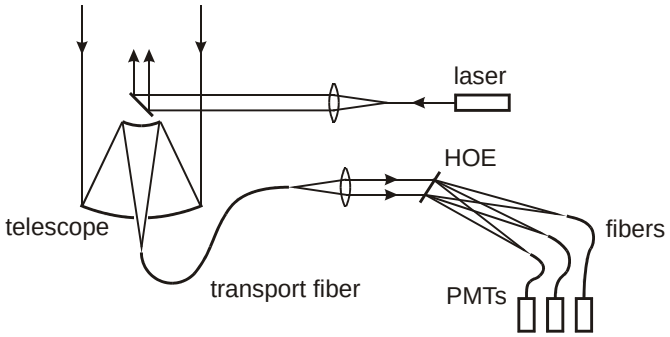

Fig. 1: The basic lidar system. A laser beam is expanded, collimated and directed into the atmosphere. The return light is collected by a transport fiber at the focus of the telescope. The light exiting the fiber is collimated and passed through the HOE to isolate RRS and Rayleigh light into individual fibers for photon counting in photomultiplier tubes (PMTs).

Each of the fibers carries the light from a particular spectral line into a separate photomultiplier tube (PMT) for photon counting. The signal received by each PMT is time-gated into altitude bins, with the entire record integrated over many laser pulses. In the case of the rotational Raman lidar, the relative magnitude of several spectral lines in each altitude bin allows determination of the absolute temperature at a given altitude. For a Rayleigh lidar, the variation in the relative signal strength with altitude, along with a suitable atmospheric model, provides the measurement of temperature.

2. The holographic optical element

The fabrication of holographic lenses has been discussed in many texts[9, 10, 16-19], but we will briefly outline the construction and performance of the HOE we have designed for this lidar. The recording and reconstruction of the holographic lens is shown in Figure 2. A laser is spit into two beams: The first is spatially filtered to produce a divergent "object" beam normal to the holographic medium [Fig. 2a]. The second, "reference" beam is spatially filtered, collimated and made to intersect the object beam at some angle to the plate. The hologram is a recording of the interference pattern formed between these two beams. After the hologram has been exposed and developed, the processed film is replaced in its recording position [Fig. 2b]. The phase-conjugate of the original reference beam (also a plane wave) illuminates the hologram to reconstruct a convergent object beam.

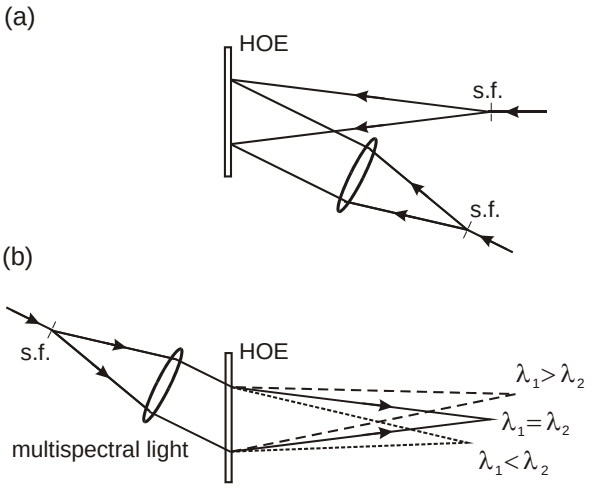

Fig. 2: a. Recording. The hologram is recorded between a divergent beam (from spatial filter, s.f.) perpendicular to the plate and a plane wave reference beam incident from an angle. **b.** Reconstruction. The phase conjugate reference beam at wavelength λ_2 will focus at a different spatial location relative to the recording wavelength (λ_1).

A change in the wavelength of the reconstructing reference beam will result in a change in the focal length of the HOE, as well as lateral shift in the location of the focus. Given a recording wavelength and focal length (λ_1, f_1), the focal length (f_2) at a replay wavelength of (λ_2) is given by:

$$f_2 = \frac{\lambda_1}{\lambda_2} f_1 . \qquad (1)$$

For our on-axis object beam configuration, the reconstructed angle (ϕ_2) is related to the recording angle (ϕ_1) by:

$$\sin(\phi_2 - \phi_1) = (1 - \lambda_1/\lambda_2)\sin\phi_1 . \qquad (2)$$

The HOE only produces a diffraction-limited focus over a limited bandwidth, centered about the recording wavelength. At more extreme wavelengths, the appearance of off-axis aberrations, particularly coma, will degrade the quality of the focus[16-19]. The greater

the dispersion (as determined by the angular separation of the recording beams), the smaller the useable, unaberrated bandwidth.

Using cw, frequency-doubled Nd:YAG laser (λ = 532.075nm), we constructed a phase hologram on bleached Agfa 8E56-plate film with a diffraction efficiency of about 35%, using a 35^{o} angle between the recording beams. The 80mm-diameter HOE was written using a 500mm focal length collimating lens and a point source 500mm from the plate, to give no overall system magnification. With the phase conjugate reference beam incident on the HOE, a focused beam was reconstructed to form a diffraction-limited focal spot. The reconstruction was next made with a green-HeNe laser (λ = 543.516nm), which also produced an unaberrated focal spot. Diffraction-limited reconstruction over a bandwidth of 11.5nm is more than enough to accommodate all the lines of interest in the RRS. The focal spot of the green-HeNe lay at a lateral distance of 6.92mm relative to the focal spot at the recording wavelength, and 10.06mm closer to the HOE, which is in agreement with Eqs. (1) and (2). Based on these measurements, the spectral resolution limit in the lateral direction, using point-source illumination, is $\Delta\lambda$ = 0.06Å, which corresponds to Δf = 6.4GHz and $\Delta\omega$ = 0.21cm^{-1}. In order to gather light from particular spectral lines, the collection fibers must be aligned along an angled focal plane. This arrangement is depicted in Figure 3, with the fiber locations for the Rayleigh line and the J=6, 16 and 20 nitrogen Anti-Stokes RRS lines positioned from right to left. These particular lines were chosen due to their large isolation from neighboring lines.

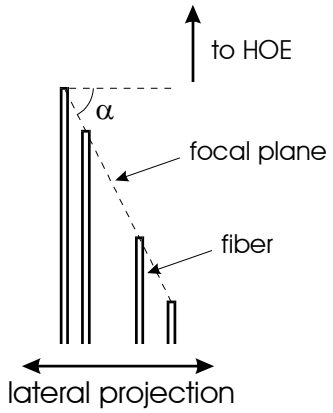

Fig. 3: Fiber positioning. The fibers are placed along an angled focal plane to collect the focused light at each RRS line. Shown here are the fibers for the J=20, 16 and 6 RRS lines, along with another for the Rayleigh line (left to right).

There are two HOE properties that must be precisely known for optimum performance of the lidar: resolution using fiber input/output, and diffuse scattering by the holographic substrate. In our analysis of the hologram performance, above, we quoted a resolution limit based on point-source illumination. A spatial filter provided this illumination, but the same result could be achieved by using a single mode fiber. In our lidar system, we will be using multimode optical fibers (to increase the amount of backscattered light collected), which reduces the resolution of the HOE in the same way as increasing the slit-size on a spectrometer. Using a 50μm (NA=0.08) transport fiber, for example, gives a resolution of 0.92Å. This decrease in resolution will still provide isolation of individual

lines in the nitrogen RRS spectrum while ensuring that the lidar is insensitive to pressure broadening of the lines[20, 21]. In order to verify this, we passed a cw, frequency-doubled Nd:YAG laser through a cell of nitrogen gas at 10 atmospheres. A lens was used to gather the light scattered at right angles to the beam path, and focus it into a 50μm (NA=0.08) multimode transport fiber, and a second, 50μm (NA=0.37) multimode fiber was scanned along the focal plane of the HOE. Figure 4 shows the anti-Stokes RRS spectrum measured in this experiment, clearly demonstrating the ability of the HOE to isolate individual lines.

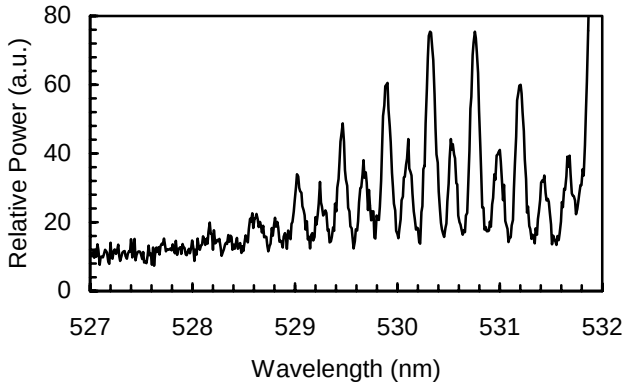

Fig. 4: RRS spectrum. This shows a plot of the nitrogen, anti-Stokes RRS spectrum made by scanning a 50μm multimode fiber along the focal plane of the HOE. The excitation laser (532nm) was directed into a nitrogen cell at 10 atmopsheres.

When the reconstructing beam strikes the hologram, defects in the emulsion scatter a small portion of the incident light into all directions. This results in cross-talk between channels in the RRS spectrum and the intense Rayleigh/Mie return at lower altitudes, leading to an error in the measured strength of each RRS line. Figure 5 shows the relative intensity of scattered radiation with lateral distance at the focal plane of the HOE, as collected by a 50μm multimode fiber.

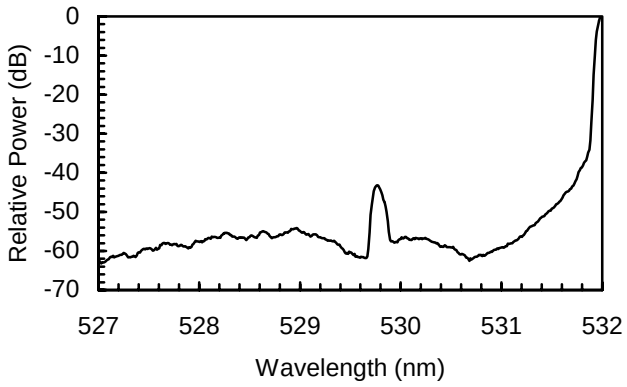

Fig. 5: Scattered light. The plot of the relative power scattered into a 50μm multimode fiber along the focal plane of the HOE illuminated by the recording laser (λ = 532nm). The secondary peak near 530nm results from a front back reflection within the hologram.

This plot can be used to estimate the scattering contribution expected at the chosen RRS line, from other lines. For example, the scatter from the Rayleigh/Mie return will contribute about 10^{-6} of its total counts into the J=6, 16 and 20 RRS channels. The amount of Rayleigh/Mie scattering is about 10^3 larger than the RRS for altitudes greater than 3km and less than 70km (contributing to 0.1% of the measured RRS counts)[22], and about $3x10^4$ larger than the RRS for altitudes under 2km (about 3% of measured counts)[23]. The scattering in the HOE can be further reduced by using an alternative holographic medium such as dichromated gelatin, and by adding anti-reflection coatings to the glass substrate. However, by simply measuring the counts in the Rayleigh/MIE channel, the scattering contribution into each of the other channels can be calculated and subtracted from their measured values with a slight increase in the overall error.

3. Lidar models

We have constructed a predictive model of a thermal Raman/Rayleigh lidar, which incorporates the holographic optical element as shown in Figure 1. A pulsed, single-frequency, frequency-doubled Nd:YAG laser (100Hz, 0.2J/pulse, λ = 532.075nm, 3ns pulse width) is expanded to 0.1m-diameter and directed into the atmosphere. The backscattered return light is gathered by a telescope (D = 0.41m, f = 4.1m) and directed into a 50μm low numerical aperture (NA = 0.08) multimode transport fiber. Three individual 50μm (NA =0.37) multimode fibers are located at the precise foci of particular spectral lines. The image produced by the telescope will change in both size and position depending on the altitude, which will change the amount of light coupling into the multimode transport fiber[24]. Due to diffraction, the beam diameter will increase from its initial diameter of 0.1m and thus change the size of the image spot produced by the telescope. If the 50μm fiber is placed at the image position for 8km altitude, the corresponding image size is identical to the fiber core diameter. Above 8km, the laser spot size increases linearly with altitude and the image spot size is inversely proportional to altitude, while the change in image distance is negligible. These competing effects result in all light above 8km being coupled into the fiber. For light returning from lower altitudes, we have defined the telescope factor (ε) to be the ratio of the area of the fiber core to the area of the image spot at the position of the fiber.

3.1 Raman lidar

To calculate the backscatter cross-section and RRS spectrum, we have followed the same procedure used by various other authors. The differential scattering cross-section (in m^2sr^{-1}) is given by[3]:

$$\sigma_b = \frac{112\pi^4}{45}\omega_r{}^4\gamma^2 F_J b_{J-J'} \tag{3}$$

where ω_r is the wavenumber of the anti-Stokes Raman-shifted line given by:

$$\omega_r = \omega_o + 2B(2J-1) - 4D_o\left(2J^3 - 3J^2 + 3J - 1\right) \tag{4}$$

with the rotational constants B_o and D_o. F_J is the fraction of molecules in rotational state J and $b_{J-J'}$ is the Placzek-Teller coefficient for the anti-Stokes region of the RRS. Note, the anti-Stokes region is chosen in order to avoid the effects of fluorescence, which can pollute the number of counts in the Stokes lines[4]. The values of F_J and $b_{J-J'}$ can be calculated using[25]:

$$F_J \cong \frac{g_J(2J+1)\exp(-E_J/kT)}{(2I+1)^2\, kT/2hcB_o} \tag{5}$$

$$b_{J-J'} = \frac{3J(J-1)}{2(2J+1)(2J-1)} \tag{6}$$

where

$$E_J = J(J+1)hcB_o - D_o hcJ^2(J+1)^2 \tag{7}$$

and c, h, k are the speed of light, Planck's constant, and Boltzmann's constant respectively, and T is the temperature of the gas. The constants for the nitrogen and oxygen molecular species are given in Table 1. From these equations, the back-scattered cross-section of each line in the RRS spectrum can be determined and are shown in Figure 6. Note that the only variables affecting the relative strength of each line are the selection rules and the Boltzmann factor given in Eq. 5.

Constant	N_2	O_2
I (ref 3)	1	0
g_J (even J, odd J) (ref 3)	6, 3	0, 1
D_o ($\times 10^{-4}$ m^{-1}) (ref 5, 25)	5.48 ± 0.05	4.85 ± 0.01
B_o (m^{-1}) (ref 5, 26)	198.950 ± 0.002	143.768 ± 0.001
γ^2 ($\times 10^{-60}$ m^6) (ref 3, 27)	0.52 ± 0.04	1.4 ± 0.1

Table 1: A summary of molecular constants for N_2 and O_2.

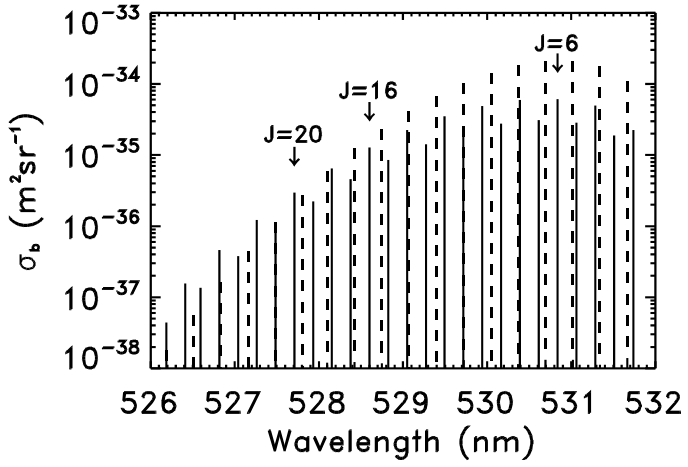

Fig. 6: The predicted rotational Raman spectrum. A plot of the 250K, RRS anti-Stokes backscattered cross-section (σ_b) for both O_2 (dashed) and N_2 (solid), at an excitation wavelength of 532.075nm. The N_2 lines at J = 6, 16 and 20 are indicated.

Due to the fact that g_J is zero for the even-J O_2, there are several lines for the nitrogen spectrum that are well isolated from neighboring lines. For the present discussion we have selected the J = 6, 16 and 20 rotational states of the nitrogen spectrum, (λ = 530.839nm, 528.610nm and 527.727nm, respectively) as these were isolated lines which provided the best sensitivity over a range of temperatures. While a greater number of lines may be used, for this initial calculation we limited ourselves to these three.

We can predict the photon count (PC) for each of the lines by using the following equation:

$$PC = \kappa \frac{nN\varepsilon\sigma_b A\eta\tau^2\Delta z}{z^2} \tag{8}$$

where;

κ is the fractional amount of the molecular species (= 0.78 for N_2),
n is the number of photons being radiated (30mins, 100Hz, 0.2J/pulse),
N is the number density of the atmosphere ($\approx 2.5\times10^{25}\exp(-z/7040)$ m^{-3}),
ε is the telescope form factor (discussed above),
A is the collector area (= 0.12m^2),
η is the efficiency of the entire optical system[28] (= 0.03),
τ is the transmission of the atmosphere[29] (= $0.583\exp(0.539\exp(-z/4.907))$),
Δz is the altitude bin size (= 250m), and
z is the altitude in meters above ground level.

Equation 8 predicts the expected photon counts for each line at a given temperature (based on the ICAO standard atmosphere), but in reality there will be fluctuations in these numbers due to counting statistics. We simulated real data values by randomizing the number of counts in each line according to Poisson statistics. A temperature was calculated by a least-squares fit of Eq. (8) to this "data", and from many "runs" we obtained a variance in these temperatures. The results are shown in Figure 7, where the standard deviation in temperature is plotted against altitude. For this calculation we have assumed that the lidar is located at sea level.

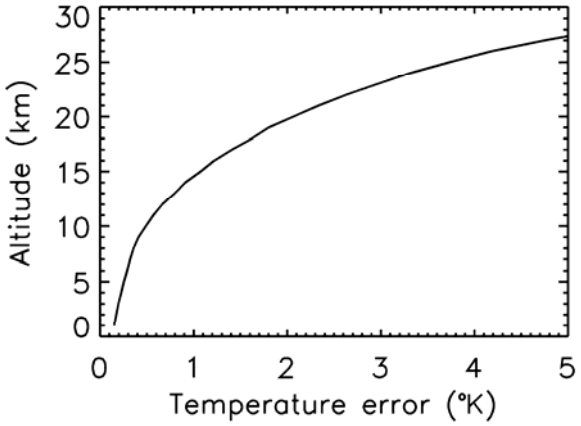

Fig. 7: Raman lidar. This plot shows the error in Raman temperature with altitude.

This prediction shows that temperature profiles of the atmosphere can be determined with an error of less than 1% up to altitudes of 20km. It should be noted, however, that this could be improved by optimizing the usual lidar characteristics, e.g. increasing telescope area, laser power etc. Furthermore, the temperature error from the holographic Raman lidar can also be reduced simply by selecting a greater number of nitrogen lines, or by using additional molecular species such as oxygen, as fitting parameters. It is difficult to make a direct performance comparison with other existing Raman lidars due to differences in operational parameters, but the photon counts are expected to be much higher due to the increased efficiency of the HOE compared to traditional narrowband filters. Also, since this system does not require any calibration against a radiosonde, there will not be the introduction of errors inherent in this step.

3.2 Rayleigh lidar

Laser light is elastically backscattered by the air molecules, and is collected by the telescope. The photon-count per laser pulse from the Rayleigh backscatter is simply:

$$S(z) = Nn\beta_r \Delta z \frac{A}{4\pi\ z^2} \eta\tau^2 \tag{9}$$

where;

N is the number density of the air molecules,
n is the number of photons in a laser pulse,
β_r is the backscatter cross section of the air molecules
Δz is the altitude bin size,
A is the area of the telescope,
z is the altitude above ground level,
η is the efficiency of the optical detection system (given above), and
τ is the transmission of the atmosphere as given above.

Using data collected by the lidar telescope, one can solve for the number density of the air molecules. By assuming a hydrostatic equilibrium throughout the atmosphere,

combined with the ideal gas law, integrating the resulting equation downwards from the top (z_{Top}) of the atmosphere will give a temperature profile[11-15]:

$$T(z_i) = \frac{1}{\rho(z_i)}\left[\rho_{Top}T_{Top} + \frac{M\Delta z}{k_B}\sum_{z_i}^{z_{Top}-1}\rho\left(z_i + \frac{\Delta z}{2}\right)\, g\left(z_i + \frac{\Delta z}{2}\right)\right] \tag{10}$$

given

$$\rho = \frac{Nm_a}{N_A} \qquad \text{and} \qquad g = \frac{GM_E}{(z + R_E)^2} \tag{11}$$

where;

M is the mass of the air in kg,
k_B is Boltzmann's constant,
ρ is the mass density of the air molecules,
N_A is Avogadro's number,
m_a is the atomic mass of air in atomic mass units,
g is the acceleration due to gravity, and
R_E and M_E are the mean radius and mass of the Earth, respectively.

We modeled the performance of the Rayleigh lidar with the same system properties[30, 31] (532nm laser with 0.25J/pulse @ 100Hz, 30min integration time, 16-inch telescope) and statistical analysis procedures as used for the Raman lidar. The results, shown in Figure 8, indicate that even with a small telescope, Rayleigh temperature profiles can be extended up to 60km above a lidar located at sea level, with less than a 5^{o}K error. Once again, however, higher accuracy and altitudes can be achieved by improving the standard system properties. With differences in operational parameters taken into account, the performance of the holographic Rayleigh lidar is comparable to other existing lidars.

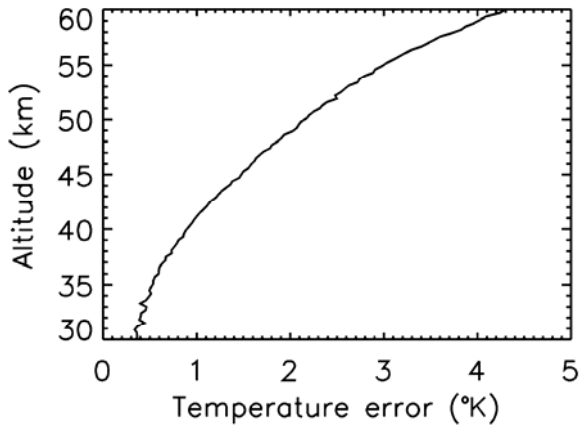

Fig. 8: Rayleigh lidar. This plot shows the error in Rayleigh temperature with altitude.

3.3 Further lidar applications

As a result of our analysis of the lidar performance, we have discovered two possible enhancements; daytime operation and aerosol content measurements. The narrow bandwidth of the HOE makes it possible to reduce the daytime background counts to levels comparable to the expected Raman and Rayleigh photon counts. Once this

background is subtracted from the signal, a daytime measurement is possible with a minor increase in the error. However, the scattering in the HOE must be reduced by several orders of magnitude compared to current levels. We are investigating the application of fixation-bleach techniques for the silver halide sensitized gelatin holograms, as well as dichromated gelatin, to obtain these improvements.

The lidar system may also be adapted for absolute aerosol content measurements. Below ~30km, the Rayleigh backscatter signal can be contaminated by Mie scattering off aerosols, which occurs at the same wavelength. However, since there is negligible Mie scattering at the rotational Raman wavelengths (with only an absorption component to be considered[15]), a comparison of the relative strengths of the RRS and Rayleigh photon counts should provide a good measure of the total aerosol content.

4. Conclusion

We have proposed using a simple holographic optical element (HOE) in a lidar to efficiently isolate both rotational Raman and Rayleigh backscattered light. At low altitudes, the relative strengths of lines in the rotational Raman scattering spectrum can be used to calculate an absolute temperature of the atmosphere. At higher altitudes, the Rayleigh signal can determine temperature in the traditional manner. We have constructed a HOE and found it capable of isolating the relevant spectral components with high efficiency. Our models predict that a holographic Raman/Rayleigh lidar would be capable of measuring atmospheric temperature profiles to within 2% from ground to 60km, with a 16-inch aperture. This is an improvement on existing rotational Raman lidars while giving similar performance to existing Rayleigh lidars. However, the ability to perform both measurements with a single instrument, and the prospect of using the Raman measurements as a boundary condition on the Rayleigh measurements should make this a very useful instrument. We are presently constructing a lidar system incorporating our HOE, to test the validity of our theory and evaluate the performance of a real device.

Acknowledgements

We would like to acknowledge the support of this research by the US Air Force Office of Scientific Research and the US Air Force Academy.

References

1. J. Cooney, " Measurement of atmospheric temperature profiles by Raman backscatter," J. Appl. Meteorol. **11**, 108-112 (1971).
2. A. Cohen, J. A. Cooney and K. N. Geller, "Atmospheric temperature profiles from measurements of rotational Raman and elastic scattering," Appl. Opt. **15**, 2896-2901 (1976).
3. C. M. Penney, R. L. St. Peters and M. Lapp, "Absolute rotational Raman cross-sections for N_2, O_2 and CO_2," J. Opt. Soc. Am. **64**, 712-716 (1974).

4. D. Nedeljkovic, A. Hauchecorne and M. L. Chanin, “Rotational Raman lidar to measure the atmospheric temperature from the ground to 30km,” IEEE Trans. Geosci. Rem. Sens. **31**, 90-101 (1993).
5. G. Vaughan et al., “Atmospheric temperature measurements made by rotational Raman scattering,” Appl. Opt. **32**, 2758-2764 (1993).
6. P. A. T. Haris and C. R. Philbrick, “Rotational Raman lidar for temperature measurements in the troposphere,” Proc. IEEE Topical symposium on combined optical-microwave Earth and atmospheric sensing, Atlanta, 141-144 (1995).
7. J. Zeyn, W. Lahmann and C. Weitkamp, “Remote daytime measurements of tropospheric temperature profiles with a rotational Raman lidar,” Opt. Lett. **21**, 1301-1303 (1996).
8. G. E. Walrafen, “Slitless optical-fiber laser-Raman spectrometer employing a concave holographic grating,” Appl. Spectrosc. **31**, 295-298 (1977).
9. J. K. Brasseur, G. Andersen, P. A. T. Haris and R. J. Knize, “Daytime holographic Raman lidar system,” Proc. SPIE **4035**, *Laser Radar Technology and Applications V*, 13-21 (2000).
10. T. A. Berkoff et al. “Remote detection of Raman scattering by use of a holographic optical element as a dispersive telescope,” Opt. Lett. **25**, 1201-1203 (2000).
11. G. S. Kent and R. W. H. Wright, “A review of laser radar measurements of atmospheric properties,” J. Atmos. & Terres. Phys. **32**, 917-943 (1970).
12. A. Hauchecorne and M.-L. Chanin, “Density and temperature profiles obtained by lidar between 35 and 70km,” Geophys. Res. Lett. **7**, 565-568 (1980).
13. R. J. Sica, et al., “Lidar measurements taken with a large-aperture liquid mirror. 1. Rayleigh-scatter system,” Appl. Opt. **34**, 6925-6936 (1995).
14. T. Leblanc, I. S. McDermid, A. Hauchecorne, P. Keckhut, “Evaluation of optimization of lidar temperature analysis algorithms using simulated data,” J. Geophys. Res. **103**, 6177-6187 (1998).
15. M. R. Gross et al., “Temperature measurements made with a combined Rayleigh-Mie and Raman lidar,” Appl. Opt. **36**, 5987-5995 (1997).
16. M. J. R. Scwar, T. P. Pandya and F. J. Weinberg, “Point holograms as optical elements,” Nature **215**, 239-241 (1967).
17. R. W. Meier, “Magnification and third-order aberrations in holography,” J. Opt. Soc. Am. **55**, 987-992 (1965).
18. Y. Amitai, A. A. Friesem and V. Weiss, “Designing holographic lenses with different recording and readout wavelengths,” J. Opt. Soc. Am. A. **7**, 80-86 (1990).
19. *Optics of diffractive and gradient-index elements and systems*, G. I. Greisukh, S. T. Bobrov and S. A. Stepanov, (SPIE, Bellingham, Washington, 1997).
20. G. C. Herring and W. K. Bischel, “Model of the rotational Raman gain coefficients for N_2 in the atmosphere,” Appl. Opt. **26**, 2988-2994 (1987).
21. I. D. Ivanova, L. L. Gurdev and V. M. Mitev, “Lidar technique for simultaneous temperature and pressure measurement based on rotational Raman scattering,” J. Mod. Opt. **40**, 367-371 (1993).
22. P. Keckhut, A. Hauchecorne and M. L. Chanin, “A critical review of the database acquired for the long-term surveillance of the middle atmosphere by the French Rayleigh lidars,” J. Atmos. and Oceanic Tech. **10**, 850-867 (1993).

23. C. Y. She, R. J. Alvarez II, L. M. Caldwell and D. A. Krueger, "High-spectral-resolution Rayleigh-MIE lidar measurement for aerosol and atmospheric profiles," Opt. Lett. **17**, 541-543 (1992).
24. J. R. Jenness, Jr., D. B. Lysak, Jr. and C. R. Philbrick, "Design of a lidar receiver with fiber-optic output," Appl. Opt. **36**, 4278-4284 (1997).
25. G. Hertzberg, *Molecular spectra and molecular structure, vol. I – spectra of diatomic molecules, 2nd ed.*, 124-125, (Krieger, Malabar, Florida, (1989).
26. Y. Arshinov and S. Bobrovnikov, "Use of a Fabry-Perot interferometer to isolate pure rotational Raman spectra of diatomic molecules," Appl. Opt. **38**, 4635-4638 (1999).
27. γ^2 of Reference 3 is for and excitation wavelength of 488nm. Because this value is common to all of the Nitrogen RRS lines, the precise value is not necessary to determine the temperature our scheme. Thus, we have used the quoted value for 488nm.
28. The equation for the transmission of the atmosphere is based on a numerical fit to a low-aerosol content, mid-latitude, springtime LOWTRAN atmosphere at the laser wavelength.
29. The overall optical efficiency value was estimated from the product of the efficiencies for the telescope-fiber coupling (90%), the HOE itself (35%), the coupling into the individual fibers (90%) and the PMTs (10%).
30. For the Rayleigh model the MSIS-E-90 Model Atmosphere was used instead of the ICAO standard used for the Raman model. The numbers were generated using online software available at http://nssdc.gsfc.nasa.gov/space/model/atmos/msise.html, and based on Reference 27.
31. A. E. Hedin, "Extension of the MSIS thermosphere model into the middle and lower atmosphere," J. Geophys. Res. **96**, 1159-1172 (1991).